

This is an Open Access document downloaded from ORCA, Cardiff University's institutional repository: <https://orca.cardiff.ac.uk/id/eprint/122305/>

This is the author's version of a work that was submitted to / accepted for publication.

Citation for final published version:

Jian, Yanfei, Yu, Tingting, Jiang, Zeyu, Yu, Yanke, Douthwaite, Mark, Liu, Jingyin, Albilali, Reem and He, Chi 2019. In-depth understanding of the morphology effect of α -Fe₂O₃ on catalytic ethane destruction. *ACS Applied Materials and Interfaces* 11 (12) , pp. 11369-11383. 10.1021/acsami.8b21521

Publishers page: <http://dx.doi.org/10.1021/acsami.8b21521>

Please note:

Changes made as a result of publishing processes such as copy-editing, formatting and page numbers may not be reflected in this version. For the definitive version of this publication, please refer to the published source. You are advised to consult the publisher's version if you wish to cite this paper.

This version is being made available in accordance with publisher policies. See <http://orca.cf.ac.uk/policies.html> for usage policies. Copyright and moral rights for publications made available in ORCA are retained by the copyright holders.



In-Depth Understanding of the Morphology Effect of α -Fe₂O₃ on Catalytic Ethane Destruction

Yanfei Jian,^{†,○} Tingting Yu,^{‡,○} Zeyu Jiang,[†] Yanke Yu,^{†,§} Mark Douthwaite,^{||}

Jingyin Liu,[⊥] Reem Albilali,[#] and Chi He^{*,†,||,▽}

[†]State Key Laboratory of Multiphase Flow in Power Engineering, School of Energy and Power Engineering, Xi'an Jiaotong University, Xi'an 710049, Shaanxi, P.R. China

[‡]State Key Laboratory of Heavy Oil Processing, China University of Petroleum, Beijing 102249, P.R. China

[§]Department of Chemical Engineering, Columbia University, New York, New York 10027, United States

^{||}Cardiff Catalysis Institute, School of Chemistry, Cardiff University, Main Building, Park Place, Cardiff CF10 3AT,

U.K. [⊥]Yunhui Co., Ltd., Shanghai 201199, P.R. China

[#]Department of Chemistry, College of Science, Imam Abdulrahman Bin Faisal University, P.O. Box 1982, Dammam 31441, Saudi Arabia

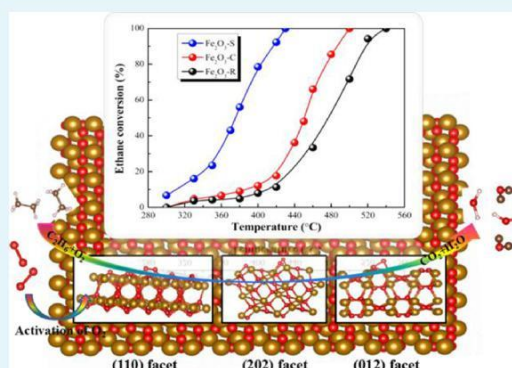
[▽]National Engineering Laboratory for VOCs Pollution Control Material & Technology, University of Chinese Academy of Sciences, Beijing 101408, P.R. China

* Supporting Information

ABSTRACT: Shape effects of nanocrystal catalysts in different reactions have attracted remarkable attention. In the present work, three types of α -Fe₂O₃ oxides with different micromorphologies were rationally synthesized via a facile solvothermal method and adopted in deep oxidation of ethane. The physicochemical properties of prepared materials were characterized by XRD, N₂ sorption, FE-SEM, HR-TEM, FTIR, in situ DRIFTS, XPS, Mössbauer spectroscopy, in situ Raman, electron energy loss spectroscopy, and H₂-TPR. Moreover, the formation energy of oxygen vacancy and surface electronic structure on various crystal faces of α -Fe₂O₃ were explored by DFT calculations. It is shown that nanosphere-like α -Fe₂O₃ exhibits much higher ethane destruction activity and reaction stability than nanocube-like α -Fe₂O₃ and nanorod-like α -Fe₂O₃ due to larger amounts of oxygen vacancies and lattice defects, which greatly enhance the concentration of reactive oxygen species, oxygen transfer speed, and

material redox property. In addition to this, DFT results reveal that nanosphere-like α -Fe₂O₃ has the lowest formation energy of oxygen vacancy on the (110) facet ($E_{\text{Vo}}(110) = 1.97$ eV) and the strongest adsorption energy for ethane (-0.26 eV) and O₂ (-1.58 eV), which can accelerate the ethane oxidation process. This study has deepened the understanding of the face-dependent activities of α -Fe₂O₃ in alkane destruction.

KEYWORDS: Fe₂O₃, oxygen vacancy, ethane, catalytic oxidation, DFT calculation



1. INTRODUCTION

The emission of volatile organic compounds (VOCs) during industrial processes leads to great environment hazards such as ozone depletion and photochemical smog.¹ Furthermore, many VOCs are carcinogenic and toxic. It is difficult to destroy linear short-chain alkanes. Ethane is an inert alkane that vastly existed in natural gas (1.8–5 mol %) and currently mainly used as a fuel for industrial refining processes.² Catalytic combustion can be considered as one of the most effective approaches for the low-energy elimination of VOCs.³ The Pt- and Pd-based materials are the most efficient catalysts for total oxidation of hydrocarbons currently, but the use of noble metal-free metal oxides offers considerable economic advantages.⁴ Among them, CoO_x, MnO_x, and FeO_x materials

constitute another choice to Pt/Pd-based catalysts. However, common CoO_x, MnO_x, and FeO_x oxides are less active than the supported noble metal catalysts in most cases. Comparatively, the environment-friendly FeO_x oxides possess much higher anti-sintering ability than the CoO_x and MnO_x materials, which suffer from catalytic deactivation at elevated temperatures, endowing FeO_x oxides a kind of promising catalysts for inert alkane destruction, although the low-temperature activity of FeO_x is more or less lower than that of CoO_x and MnO_x catalysts.^{5–7} Hematite (α -Fe₂O₃), based

on hexagonal close packing of oxygen with iron in two-thirds of the octahedral vacancies, is generally adopted as an heterogeneous catalyst due to its high resistance, low cost to deactivation, and environment-friendly properties.⁹

Controlling the morphology of the nanoparticles can influence their catalytic performance because the different topographies of the particles can expose different crystal faces.¹⁰ It is known that facet engineering causes different chemical and physical properties in nanomaterials due to distortion of the electronic structures and various exposed atoms in crystal surfaces having different exposed faces. Many applications, for example, gas sensing, energy conversion and storage, and heterogeneous catalysis are very alive to surface structures. As such, the promise of high energy and reactivity in engineering surface structures and exposure-specific aspects is becoming a promising research direction.¹¹ Different kinds of nanomaterials with special forms and structures, for example, nanowires,¹² nanorods,¹³ nanotubes,¹⁴ nanobelts,¹⁵ nano-plates,¹⁶ and nanorings,¹⁷ have been synthesized by various methods. Li et al.¹⁸ compared the catalytic property of CeO₂ nanoparticles and CeO₂ nanorods in CO oxidation and found that the catalytic activity of CeO₂ nanorods is greater than nanoparticles because the exposed {110} and {100} planes have higher oxygen storage capacity. Similarly, Xie et al.¹⁹ proposed that CeO₂ nanorods that exposed the {110} and {001} facets show a better CO conversion efficiency than CeO₂ with {111} facets. Qiu et al.²⁰ proposed that the propane adsorption energies on different crystal facets of MnO₂ are different ($\alpha(310) > \gamma(120) > \beta(110) > \delta(001)$), which influence its propane oxidation activity. Using different methods such as thermal decomposition and hydrothermal methods synthesize α -Fe₂O₃ with different crystals.²¹ Kouotou et al.¹ found that the α -Fe₂O₃ thin film exhibits good performance toward catalytic combustion of C₃H₆. Zheng et al.⁸ found that the α -Fe₂O₃ nanoparticles that have a uniform quasi-cubic structure with six identical {110} planes exhibit outstanding catalytic performance for CO oxidation because the exposed {110} planes have a high density of Fe atoms.

In this work, three kinds of α -Fe₂O₃ with different micromorphologies and exposed facets (i.e., nanosphere-like α -Fe₂O₃ (Fe₂O₃-S), nanocube-like α -Fe₂O₃ (Fe₂O₃-C), and nanorod-like α -Fe₂O₃ (Fe₂O₃-R), respectively, with predominantly exposed (110), (202), and (012) facets) were rationally synthesized, and the synthesized catalysts were extensively characterized by different technologies including electron energy loss spectroscopy (EELS), X-ray diffraction (XRD), Fourier transform infrared spectroscopy (FTIR), high-resolution transmission electron microscopy (HR-TEM), Mössbauer spectroscopy, field-emission scanning electron microscopy (FE-SEM), X-ray photoelectron spectroscopy (XPS), Raman/ in situ Raman, and temperature-programmed reduction by hydrogen (H₂-TPR). In addition, the formation energy of oxygen vacancy and surface electronic structure on different crystal faces of α -Fe₂O₃ were studied by the density functional theory (DFT) calculations. The catalytic performance of obtained materials toward the total oxidation of ethane was studied, and the effect of oxygen vacancy, lattice defect, and crystal facets on catalyst surface chemical composition, reduction property, and catalytic performance was discussed in detail.

2. EXPERIMENTAL SECTION

The detailed experimental section is described in Text S1 (Supporting Information).

3. RESULTS

3.1. Structural Property. As shown in Figure 1, the micromorphologies of Fe₂O₃-S, Fe₂O₃-C, and Fe₂O₃-R

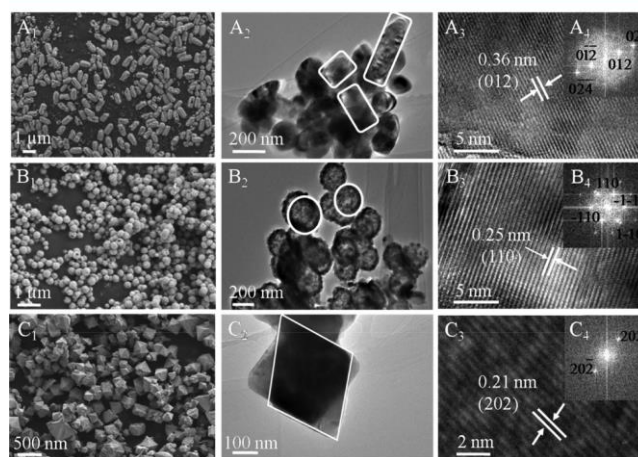


Figure 1. FE-SEM and HR-TEM images of (A, A₁, A₂) Fe₂O₃-R, (B, B₁, B₂) Fe₂O₃-S, and (C, C₁, C₂) Fe₂O₃-C (insets: FFT images of (A₃) Fe₂O₃-R, (B₃) Fe₂O₃-S, and (C₃) Fe₂O₃-C).

catalysts were determined by FE-SEM and HR-TEM. Fe₂O₃-R has a uniform diameter of 100–200 nm with a length in the range of 100–1000 nm (Figure 1A₁,A₂). A lattice spacing of 0.36 nm attributed to the (012) plane can be observed (Figure 1A₃), and similar results can be obtained from the fast Fourier transformation (FFT) of Fe₂O₃-R (Figure 1A₄). The Fe₂O₃-S sample shows a spherical morphology with a rough surface, and the average diameter of particles is 200 ± 20 nm (Figure 1B₁,B₂). Results of HR-TEM (Figure 1B₃) and FFT transformation (Figure 1B₄) confirm that Fe₂O₃-S is enclosed by the (110) planes mainly with a lattice spacing of 0.25 nm. Figure 1C₁,C₂ suggests that Fe₂O₃-C has an octahedron shape with a side size of 240 ± 10 nm. HR-TEM image (Figure 1C₃) and corresponding FFT (Figure 1C₄) reveal that the lattice fringe is 0.21 nm, implying that Fe₂O₃-C is mainly enclosed by (202) facets.

XRD patterns of prepared materials are shown in Figure 2. The diffraction peaks of Fe₂O₃-S, Fe₂O₃-C, and Fe₂O₃-R samples agree well with the α -hematite crystallographic phase of Fe₂O₃ (rhombohedral structure, JCPDS 33-0664, space group R-3c) with lattice constants of $a = 0.5035$ nm and $c = 1.3740$ nm. The lattice constants of prepared materials (Fe₂O₃-S: $a = 0.5039$ nm, $c = 1.3746$ nm; Fe₂O₃-C: $a = 0.5034$ nm, $c = 1.3750$ nm; Fe₂O₃-R: $a = 0.5038$ nm, $c = 1.3748$ nm) were calculated by the least-square fitting method, which are in accordance with the above data. The peak width at half height of Fe₂O₃-S diffractions is wider than those of Fe₂O₃-C and Fe₂O₃-R, indicating that Fe₂O₃-S has a smaller grain size than Fe₂O₃-C and Fe₂O₃-R materials, in agreement with the data calculated by the Scherrer equation (average grain sizes of Fe₂O₃-S, Fe₂O₃-C, and Fe₂O₃-R are 20, 177, and 189 nm, respectively).

The specific surface area and porosity of Fe₂O₃-S, Fe₂O₃-C, and Fe₂O₃-R materials were studied by low-temperature N₂ sorption, as displayed in Figure S1 and Table 1. It can be

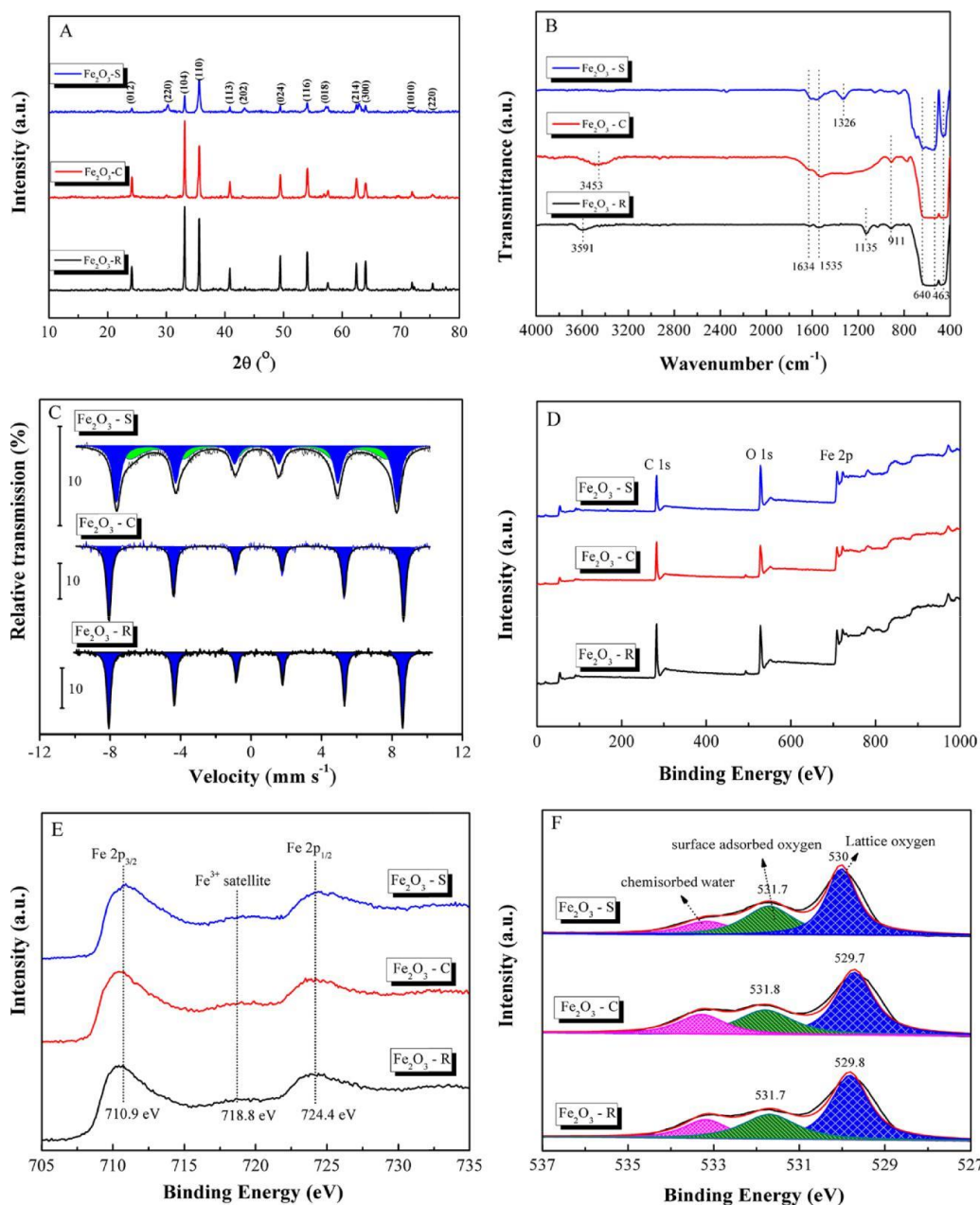


Figure 2. (A) XRD patterns, (B) FT-IR spectra, (C) room-temperature Mössbauer spectra, and (D) XPS survey spectra and corresponding (E) Fe 2p and (F) O 1s XPS spectra of prepared catalysts.

Table 1. Textural Property of Prepared Materials

sample	SBET ^a (m ² g ⁻¹)	V _t ^b (cm ³ g ⁻¹)	C _s ^c (nm)	D _p ^d (nm)	I _{H1} ^e (×10 ⁻⁴ mmol g ⁻¹ s ⁻¹)	I _{H2} ^e (×10 ⁻⁴ mmol g ⁻¹ s ⁻¹)
Fe ₂ O ₃ -S	44.5	0.11	20	7.5	1.41	1.51
Fe ₂ O ₃ -C	8.5	0.02	177	3.5	0.21	0.23
Fe ₂ O ₃ -R	8.8	0.04	189	4.7	0.14	0.18

^aSpecific surface area obtained at P/P₀ = 0.05–0.30. ^bTotal pore volume estimated at P/P₀ = 0.99. ^cCrystal size obtained from the results of XRD. ^dBJH pore diameter calculated from the desorption branch. ^eInitial H₂ consumption rates of synthesized catalysts at 340 and 350 °C.

observed in Table 1 that the specific surface area, total pore volume, and average pore diameter of Fe₂O₃-S (44.5 m² g⁻¹, 0.11 cm³ g⁻¹, and 7.5 nm, respectively) are much higher than those of Fe₂O₃-C (8.5 m² g⁻¹, 0.02 cm³ g⁻¹, and 3.5 nm, respectively) and Fe₂O₃-R (8.8 m² g⁻¹, 0.04 cm³ g⁻¹, and 4.7 nm, respectively). Figure S1A suggests that the Fe₂O₃-S sample possesses a type IV isotherm with a clear H3-type hysteresis

loop, characteristic of a mesoporous material.²² The pore size distribution (PSD) was obtained by the Barrett–Joyner–Halenda (BJH) method (Figure S1, inset). Fe₂O₃-S shows unimodal pore size distribution with a predominant pore radius of around 20 nm, indicating the homogeneous distribution of pores;²² however, Fe₂O₃-C and Fe₂O₃-R with type III isotherms can be observed (Figure S1B,C),²³ and the

pore size distribution curves of Fe₂O₃-C and Fe₂O₃-R show several mesopore peaks in the range of 15–45 nm, indicating the heterogeneity distribution of pores, which is considered to be mainly caused by an interspace between the component nanoparticles.²²

3.2. Surface Property. Figure 2B shows the FTIR spectra of Fe₂O₃-S, Fe₂O₃-C, and Fe₂O₃-R materials. All samples show a broad band at 463–640 cm⁻¹. This band can be attributed to the Fe–O bond vibration of Fe₂O₃.²⁴ The bands at 1634 and 1535 cm⁻¹ are assigned to the bending and vibration of H₂O molecules and C–O bond, respectively.²⁵ The strong absorption peaks at 3453 cm⁻¹ (over Fe₂O₃-C) and 3591 cm⁻¹ (over Fe₂O₃-R) can be assigned to the O–H stretching vibration of intermolecular hydrogen bonding,²⁵ and the weak band at 911 cm⁻¹ over Fe₂O₃-C and Fe₂O₃-R can be attributed to the vibration of Fe–OH.²⁶ For Fe₂O₃-R, the peak at 1135 cm⁻¹ can be assigned to the asymmetric and symmetric stretching vibrations of sulfonic acid group (–SO₃⁻).²⁷ The band at around 1326 cm⁻¹ over Fe₂O₃-S corresponds to the typical stretching mode of C–N heterocycles.²⁸

Figure 2C shows the room-temperature transmission Mössbauer spectra of Fe₂O₃-S, Fe₂O₃-C, and Fe₂O₃-R materials. The fitted hyperfine parameters of subspectra, for example, isomer shifts (IS), quadruple splittings (QS), magnetic hyperfine field (Bhf), and resonance half-height line widths (LW), are listed in Table 2. The Mössbauer spectrum

Table 2. Characterized Results of Synthesized Materials Obtained from the Mössbauer Spectra

sample	IS ^a (mm s ⁻¹)	QS ^b (mm s ⁻¹)	LW ^c (mm s ⁻¹)	Bhf ^d (T)	abundance (%)
Fe ₂ O ₃ -S	0.32	0.002	0.55	49.5	57.3
	0.41	0	0.49		42.7
Fe ₂ O ₃ -C	0.37	-0.15	0.31	51.9	100
Fe ₂ O ₃ -R	0.37	-0.21	0.25	51.8	100

^aIsomer shift (relative to the source). ^bQuadrupole shift/splitting.

of Fe₂O₃-S is well fitted with two sextets, and the spectra of Fe₂O₃-C and Fe₂O₃-R materials are well fitted with one sextet. The IS values of all samples listed in Table 2 are lower than 0.5 mm s⁻¹, indicating that the valence state of iron in all catalysts is +3.²⁹ The sextets with Bhf around 51 T can be assigned to the characteristic of high-spin Fe³⁺ ions in octahedral coordination of the α-Fe₂O₃ phase (hematite).³⁰ The room-temperature existence of a doublet in the Mössbauer spectrum is related to the presence of superparamagnetic nanoparticles, which have critically lower dimension based on the results of XRD (Figure 2A).³¹ The first sextet component with an IS value of 0.32 mm s⁻¹ (about 57.3%) is assigned to the presence of large hematite particles, whereas the second sextet

component with an IS value of 0.41 mm s⁻¹ (about 42.7%) is ascribed to small particles.³² In Mössbauer spectroscopy, because of the magnetic field distribution caused by local lattice distortion, the line width Γ of some spectral components is widened, and the presence of vacancies in the nearest neighbor of the Mossbauer probe or a sufficiently large impurity atom can also be observed.³² Table 2 shows that the line widths Γ of Fe₂O₃-S, Fe₂O₃-C, and Fe₂O₃-R are 0.55, 0.31, and 0.25 mm s⁻¹, respectively, suggesting that the amount of lattice defects in prepared materials are following the order of Fe₂O₃-S > Fe₂O₃-C > Fe₂O₃-R.

The surface chemical composition and chemical states of prepared materials were investigated by XPS, as displayed in Figure 2D–F and Table 3. The doublet peaks of Fe 2p_{1/2} and Fe 2p_{3/2} are located at around 724.4 and 710.8 eV, respectively (Figure 2E), in well agreement with typical binding energies of Fe³⁺ in Fe₂O₃.^{33,34} Besides, a satellite peak at around 718.8 eV is also attributed to the characteristic peak of Fe₂O₃.^{33,34} The binding energy between the satellite and Fe 2p_{3/2} peaks is 7.90 eV for all samples, which suggests the presence of α-Fe₂O₃,³⁴ consistent with the results of Mössbauer spectra (Figure 2C). In catalytic oxidation reactions, relative ratios and status of different oxygen species play crucial roles, and O 1s XPS spectra are shown in Figure 2F. The O 1s spectra of all materials can be divided into three peaks. The peaks located at 529.4–530.6, 530.8–532.0, and 532.1–532.2 eV can be assigned to the lattice oxygen for metal oxides (O_α), adsorbed oxygen (O_β), and surface oxygen by adsorbed water species (O_λ), respectively.^{35,36} Generally, because of the excellent fluidity of O_β, the high relative concentration of O_β on the surface of the catalyst can be correlated with the high activity in the oxidation reaction. It is shown in Table 3 that the ratios of O_β/O_α are approximately 0.72, 0.59, and 0.55 for Fe₂O₃-S, Fe₂O₃-C, and Fe₂O₃-R, respectively, suggesting that the largest amount of O_β species existed over the Fe₂O₃-S material. In addition to this, the O_α peak of Fe₂O₃-S (530 eV) shifts toward higher binding energy than those of Fe₂O₃-C (529.7 eV) and Fe₂O₃-R (529.8 eV), indicating that there are more defective oxygen sites over Fe₂O₃-S than the other materials.³⁷

We further divided and analyzed the Fe 2p_{3/2} XPS peak (Figure 2E) to get some understanding of sample characteristics, as shown in Figure 3. Four multiplet peaks (except the surface peak and pre-peak) in a bind energy range of 708–716 eV can be obtained.^{37,38} It is found that peak 1 is more intense (Figure 3D) and its peak area is larger than the second multiplet peak (peak 2) for samples. For hematite particles, the higher integral peak area and intensity of the first multiple peak (peak 1) are expected.^{37,38} The splitting indicates that some Fe³⁺ cations in hematite samples have tetrahedral coordination, and all cations in this phase should have octahedral coordination.^{37,38} It can be seen in the ratios of area between peak 1 and peak 2 (Table S1) in different catalysts; that is, the

Table 3. XPS Results of Prepared Catalysts

sample	binding energy (eV)				
	Fe ³⁺ 2p _{1/2}	Fe ³⁺ 2p _{3/2}	O _α ^a	O _β ^b	O _β /O _α ^c
Fe ₂ O ₃ -S	724.4	710.9	530 (39555.3)	531.7 (28550.2)	0.72
Fe ₂ O ₃ -C	724.4	710.8	529.7 (30264.4)	531.8 (17815.3)	0.59
Fe ₂ O ₃ -R	724.4	710.8	529.8 (48470.8)	531.7 (27038.9)	0.55

^aLattice over prepared catalysts (corresponding peak areas are listed in brackets). ^bAdsorbed oxygen over prepared catalysts (corresponding peak areas are listed in brackets). ^cPeak area ratio.

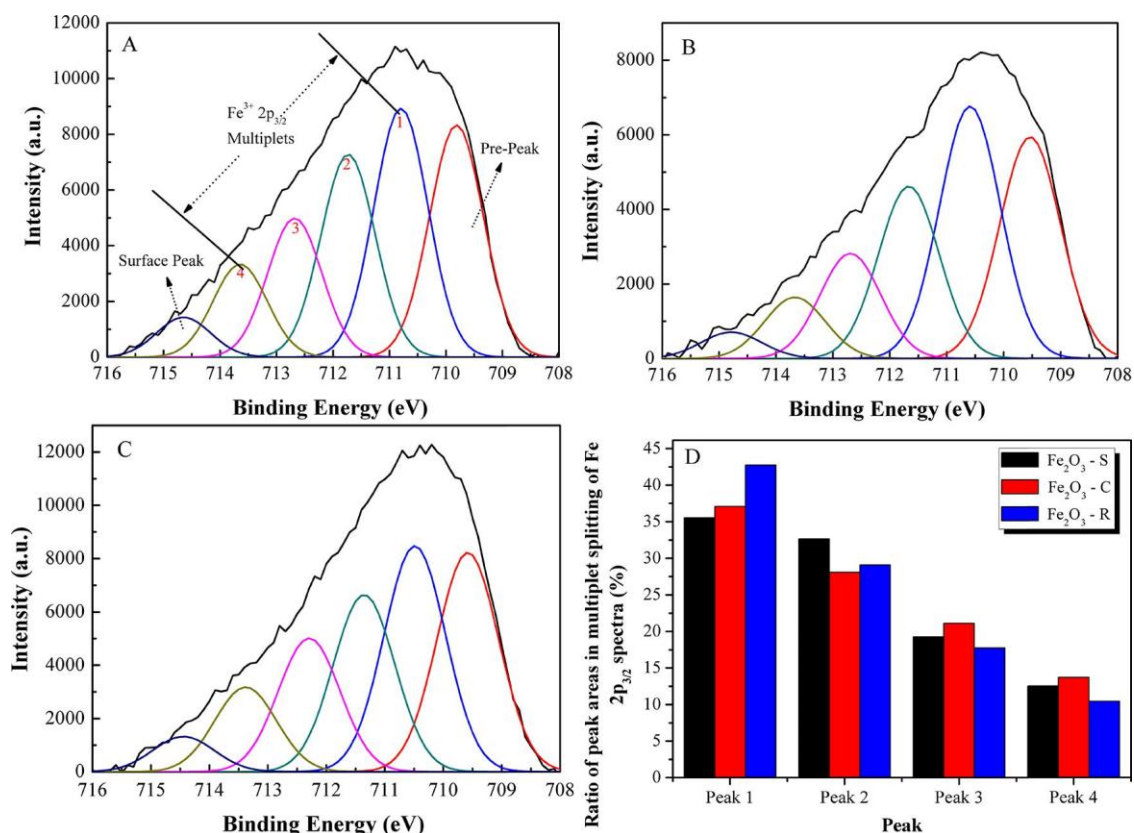


Figure 3. Analysis of the multiplet splitting of the Fe 2p_{3/2} peak of each hematite nanomaterial from the XPS results of (A) Fe₂O₃-S, (B) Fe₂O₃-C, and (C) Fe₂O₃-R. (D) Corresponding ratio of peak areas in multiplet splitting of Fe 2p_{3/2} for Fe₂O₃-S, Fe₂O₃-C, and Fe₂O₃-R.

ratio closer to 1 indicates that some of the Fe³⁺ cations are tetrahedrally coordinated in the catalyst. It is similar to γ -Fe₂O₃ where some of the Fe³⁺ cations are tetrahedrally coordinated.³⁷ It can be explained that, with nanoparticles becoming smaller, dimension-dependent structural conversion may occur, resulting in surface hematite defects and leading to the appearance of tetrahedrally coordinated Fe³⁺ cations.³⁹ As such, the Fe₂O₃-S sample with the smallest grain size (20 nm, close to the maximum diameter of defect frequency (30 nm)) possesses more defects on the surface than Fe₂O₃-C (177 nm) and Fe₂O₃-R (189 nm).

To have more details about the phase of the synthesized materials, Raman spectroscopy was utilized as shown in Figure 4. The bands at 219 and 499 cm⁻¹ are attributed to the A_{1g} mode of α -Fe₂O₃, and those observed at 286, 405, and 608 cm⁻¹ correspond to the E_g mode of α -Fe₂O₃.¹ The interactions between two magnons formed on antiparallel spins, typically of α -Fe₂O₃ (Figure 4A),⁴⁰ can lead to the appearance of the broad band between 1200 and 1400 cm⁻¹. By comparing those of Fe₂O₃-C and Fe₂O₃-R, the peaks over the Raman spectrum of Fe₂O₃-S are broader and weaker, demonstrating that the hematite nanoparticles with smaller crystalline size and long-range disordered accumulation in the structure can result in many factors such as poor crystallization, lattice defects, and oxygen vacancies.⁴¹ The Raman spectra region between 550 and 750 cm⁻¹ was extracted and further divided into three peaks (E_g of 608 cm⁻¹, LO of 660 cm⁻¹, and T of 690 cm⁻¹), as shown in Figure 4B-D. The intensity of LO and T peaks can explain that the degree of disorder in the lattice of hematite and the existence of lattice defects on the surface of nanoparticles are related, respectively.³⁷ As shown in Table

S2, the intensity of the LO band decreases in the order of Fe₂O₃-S (15.77) > Fe₂O₃-C (6.68) > Fe₂O₃-R (3.59), similar with that the T band (Fe₂O₃-S (11.42) > Fe₂O₃-C (6.55) > Fe₂O₃-R (4.70)). Above results suggest that Fe₂O₃-S has the largest amounts of structural defects than Fe₂O₃-C and Fe₂O₃-R materials, in agreement with the result of Mössbauer spectroscopy (Figure 2C).

Figure 5 shows the in situ Raman spectra of prepared Fe₂O₃ samples. It is found that the intensity of all Raman peaks decrease dramatically (becoming wider) with the increase in temperature. For hematite, the expansion of these bands is a size-dependent phenomenon caused by uneven strain broadening associated with particle size dispersion and phononic construction.⁴² Especially, the band at about 608 cm⁻¹ becomes broader and weaker for all materials due to the increase in oxygen vacancies.⁴³ Figure S2 displays the related contour map of the in situ Raman spectra of prepared materials. It can be observed that the Raman peaks of Fe₂O₃-S reduce to the minimum at only 100 °C, whereas the related temperatures for Fe₂O₃-C and Fe₂O₃-R materials are 250 and 350 °C, respectively, implying that Fe₂O₃-S is more likely to form oxygen vacancies than Fe₂O₃-C and Fe₂O₃-R. The data are collected by EELS, and a zero loss peak value on energy scale calibration was performed with a low-loss-area deconvolution to minimize the multiple scattering effect.⁴⁴ Figure 6A represents the EELS spectra of oxygen K-edge energy-loss near-edge fine structure (ELNES) for Fe₂O₃-S, Fe₂O₃-C, and Fe₂O₃-R. Four peaks, denoted as a, b, c, and d, can be found in all materials.⁴⁴ In general, a derives from the O 1s to 2p core level hybridized with the Fe 3d orbital, and b originates from the O 2p states hybridized with the transition

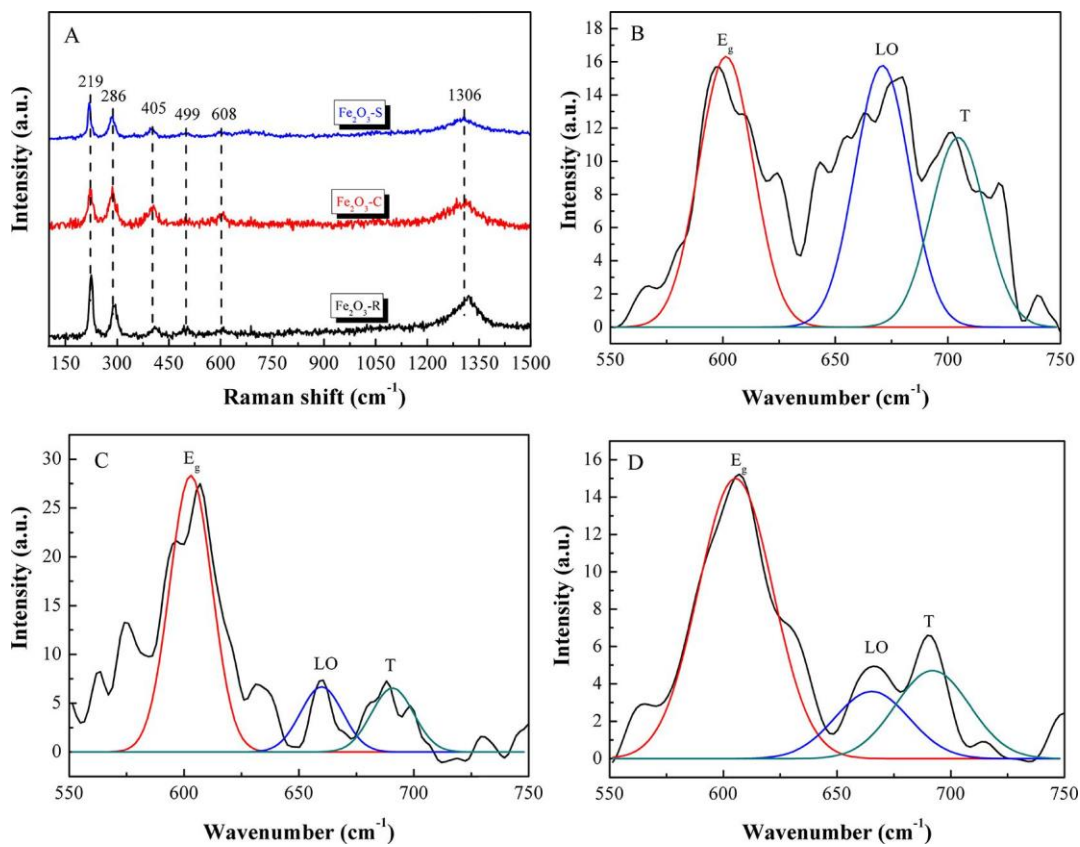


Figure 4. (A) Full Raman spectra of all hematite nanomaterials and corresponding peak deconvolution of the E_g , LO, and T bands of (B) Fe_2O_3 -S, (C) Fe_2O_3 -C, and (D) Fe_2O_3 -R samples.

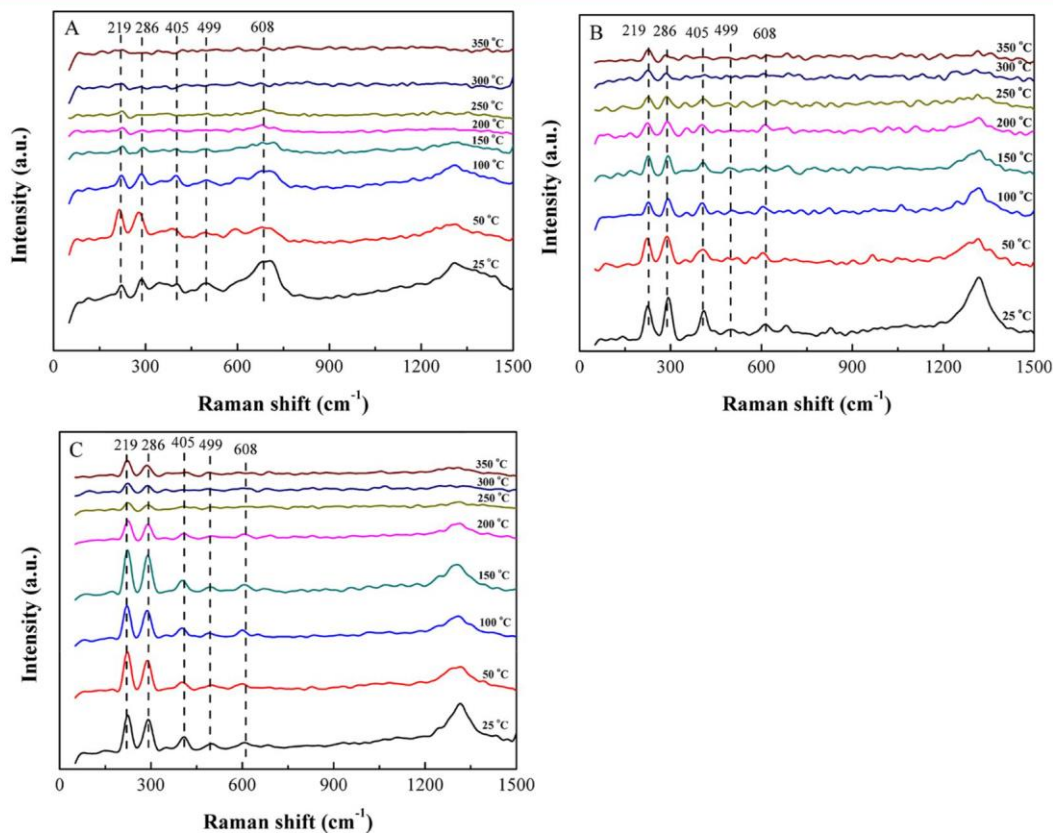


Figure 5. In situ Raman spectra of (A) Fe_2O_3 -S, (B) Fe_2O_3 -C, and (C) Fe_2O_3 -R.

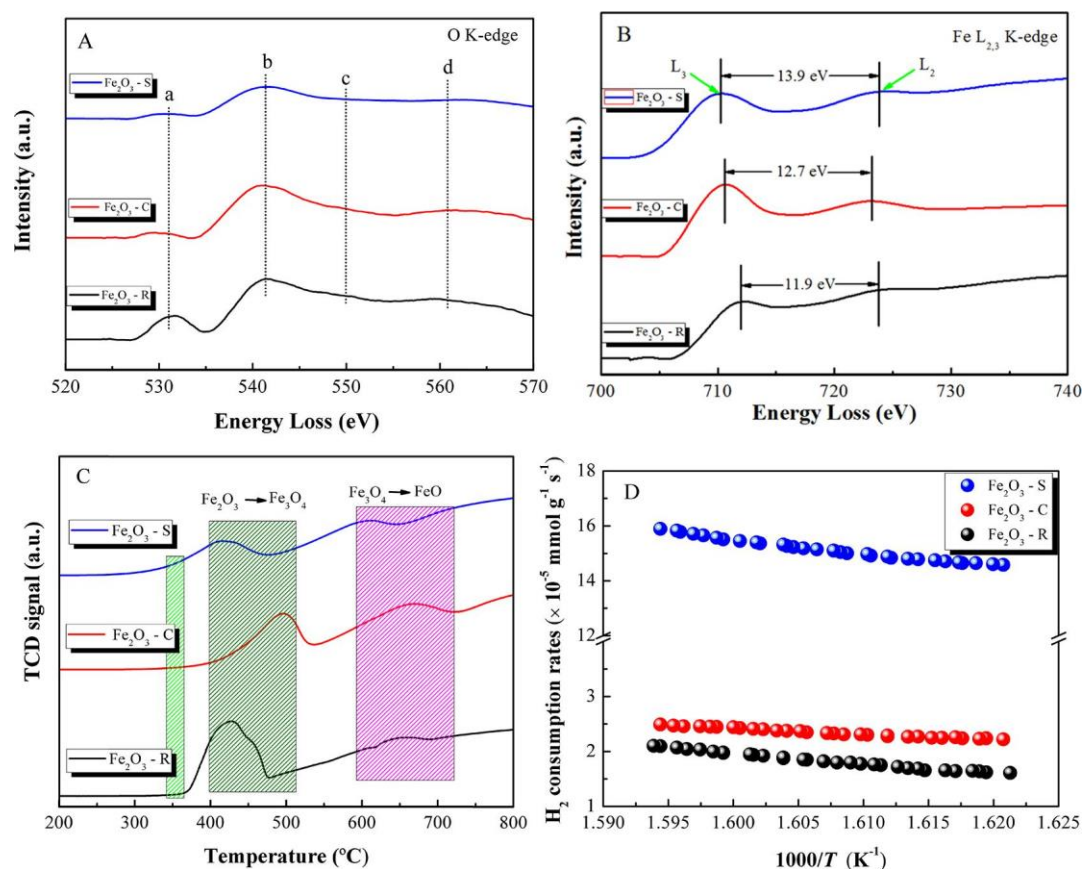


Figure 6. EELS spectra of (A) oxygen K-edge ELNES and (B) Fe L-edge of α -Fe₂O₃. (C) H₂-TPR profiles and (D) initial H₂ consumption rates of synthesized catalysts.

metal 4s and 4p states. The c and d result from the scattering of the third and first oxygen coordination shells by outgoing or backscattering electrons.^{44,45} It is obvious that the intensities of a and b of Fe₂O₃-S are lower than those of Fe₂O₃-C and Fe₂O₃-R samples (Fe₂O₃-S < Fe₂O₃-C < Fe₂O₃-R). The intensity decreases of a and b are caused by the oxygen vacancies inside the prepared materials, resulting in diminishing hybridization of metal 3d and O 2p orbitals.⁴⁴ As such, it can be demonstrated that the amount of oxygen vacancies in all materials follows the order of Fe₂O₃-S > Fe₂O₃-C > Fe₂O₃-R. The ionization state of the metal cation can be provided by the L edge via the determination of intensity and relative position of individual L₃ and L₂ edges, respectively.⁴⁴ Figure 6B represents the Fe L_{2,3} K-edge spectra of Fe₂O₃-S, Fe₂O₃-C, and Fe₂O₃-R. It can be noted that the L₃ line is the transition 2p_{3/2} → 3d_{3/2}3d_{5/2}, whereas the L₂ line refers to the transition 2p_{1/2} → 3d_{3/2}. For Fe₂O₃-S, the L₃ line is located at 710.3 eV and is separated by 13.9 eV from the L₂ line; however, the corresponding data are 710.5 and 12.7 eV and 711.9 and 11.9 eV for Fe₂O₃-C and Fe₂O₃-R, respectively. The chemical shift of L₃ lines likely results from oxygen vacancies, which partially decrease the oxidation states of Fe cations from Fe³⁺ to Fe²⁺.^{44,45} By comparing the degree of chemical shift of L₃ lines, it can be concluded that Fe₂O₃-S has the maximum amount of oxygen vacancies, followed by Fe₂O₃-C and Fe₂O₃-R, in accordance with the result of oxygen K-edge energy loss (Figure 6A).

3.3. Reducibility. Figure 6C and Figure S3 represent the H₂-TPR profiles of prepared materials, and all samples present two H₂ consumption stages due to the reduction of Fe₂O₃ to

Fe₃O₄ and Fe₃O₄ to FeO.^{36,46} The theoretical H₂ consumption amount for the reduction of Fe₂O₃ to Fe₃O₄ is 2.09 mmol g⁻¹. In the present work, the H₂ consumption amount of the first reduction stage for Fe₂O₃-S, Fe₂O₃-C, and Fe₂O₃-R samples are 2.07, 2.06 and 2.03 mmol g⁻¹, respectively, indicating that a substantial fraction of Fe³⁺ in α -Fe₂O₃ can be reduced to Fe²⁺ below 550 °C. For the purpose of comparing the reducibility at low temperature for the prepared samples, the initial H₂ consumption of the first reduction band was calculated for each sample before phase transition (the initial H₂ consumption of the first reduction band of the catalyst is less than 25%),⁴⁹ and the results are shown in Figure 6D. It can be noted that the initial H₂ consumption rate (IH₂, Table 1) of Fe₂O₃-S is much higher than those of Fe₂O₃-C and Fe₂O₃-R

with an order of Fe₂O₃-S ≫ Fe₂O₃-C > Fe₂O₃-R. For instance, the IH₂ of Fe₂O₃-S at 350 °C is 1.5 × 10⁻⁴ mmol g⁻¹ s⁻¹, over six times higher than those of Fe₂O₃-C and Fe₂O₃-R. To investigate the nature of oxygen species involved in ethane oxidation, O₂-TPD experiments were conducted. As shown in Figure S4, all samples display two desorption peaks centered at around 150 and 500 °C. The first peak (α 1-oxygen) can be attributed to the physically adsorbed oxygen or O₂⁻ (ad) species.⁴⁸ The second peak (α 2-oxygen) is associated with the desorption of chemically adsorbed oxygen O⁻ species. Generally speaking, O⁻ often belongs to the surface active oxygen,⁴⁷ and these surface reactive oxygen species are known to promote the catalytic oxidation activity.⁴⁷ Compared with the Fe₂O₃-S sample, the O₂ desorption peaks of Fe₂O₃-C and Fe₂O₃-R materials obviously shift to higher temperatures, and the intensity of these peaks is also much weaker as a result of

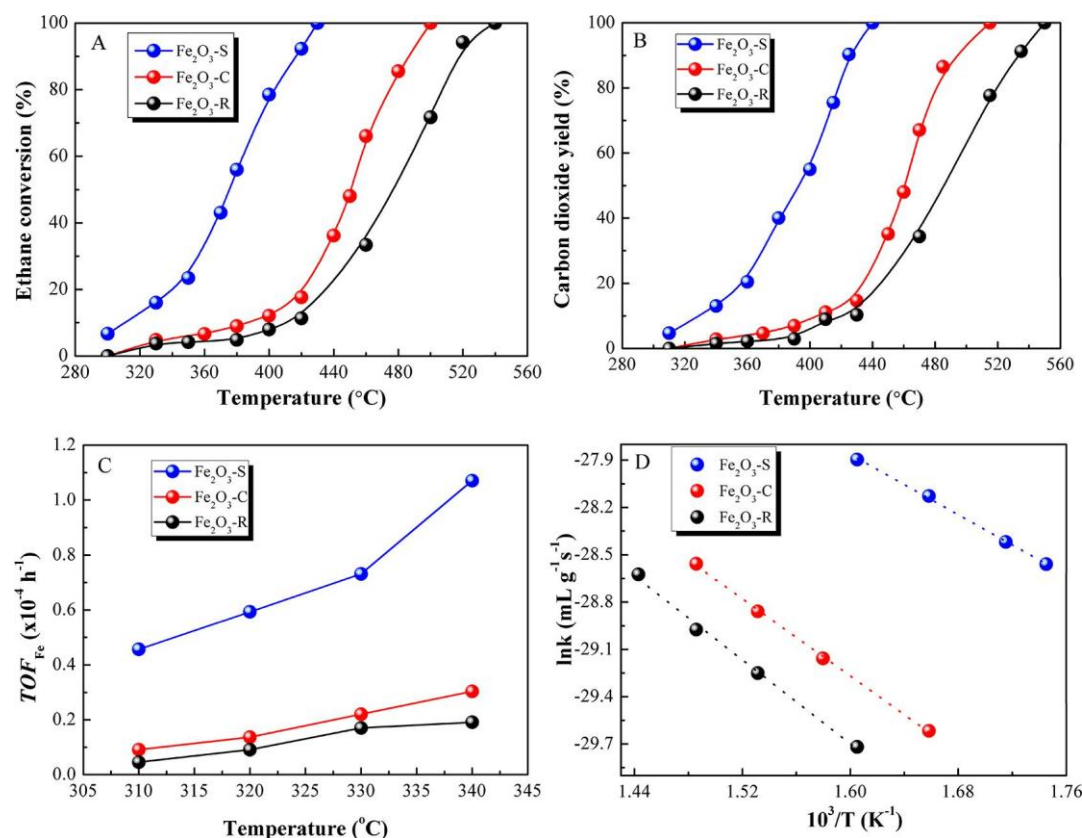


Figure 7. (A) Ignition curve, (B) CO₂ yield, (C) TOF, and (D) apparent activation energy (E_a) of different catalysts for ethane oxidation.

Table 4. Catalytic Performance of Prepared Materials for Ethane Oxidation

sample	T_{50}^a (°C)	T_{90}^a (°C)	r_1^b ($\times 10^{-3}$ mmol mL ⁻¹ h ⁻¹)	r_2^b ($\times 10^{-3}$ mmol mL ⁻¹ h ⁻¹)	TOF_{Fe1}^c ($\times 10^{-4}$ h ⁻¹)	TOF_{Fe2}^c ($\times 10^{-4}$ h ⁻¹)	E_a^d (kJ mol ⁻¹)
Fe ₂ O ₃ -S	380	415	0.46	0.67	0.73	1.07	39.7
Fe ₂ O ₃ -C	450	485	0.14	0.19	0.22	0.30	50.9
Fe ₂ O ₃ -R	480	515	0.11	0.12	0.17	0.19	55.3

^aTemperatures at 50 and 90% conversion of ethane. ^bReaction rate of ethane converted over various catalysts at 330 and 340 °C. ^cTurnover frequency based on Fe at 330 and 340 °C. ^dApparent activation energy obtained from Arrhenius plots.

the surface oxygen vacancies. Compared with the area of desorption peaks, it can be found that the amount of oxygen released from Fe₂O₃-S is much higher than those from Fe₂O₃-C and Fe₂O₃-R samples.

3.4. Catalytic Activity. Figure 7A,B reveals that the catalytic activity of prepared materials for ethane destruction follows the sequence of Fe₂O₃-S > Fe₂O₃-C > Fe₂O₃-R. Under a GHSV of 12000 h⁻¹, the Fe₂O₃-S sample can completely decompose 2500 ppm of ethane into CO₂ at 430 °C, which is significantly lower than that of Fe₂O₃-C (500 °C) and Fe₂O₃-R (540 °C). Figure 7C demonstrates that the TOF_{Fe} values of Fe₂O₃-S for ethane oxidation are much higher than those of Fe₂O₃-C and Fe₂O₃-R materials. For example, in Table 4, the calculated TOF_{Fe} values at 330 °C (0.73×10^{-4} h⁻¹) and 340 °C (1.07×10^{-4} h⁻¹) of Fe₂O₃-S are over three (0.22×10^{-4} h⁻¹ at 330 °C; 0.30×10^{-4} h⁻¹ at 340 °C) and five (0.17×10^{-4} h⁻¹ at 330 °C; 0.19×10^{-4} h⁻¹ at 340 °C) times higher than those of Fe₂O₃-C and Fe₂O₃-R, respectively, demonstrating the excellent low-temperature activity of Fe₂O₃-S for ethane destruction. In addition to this, further introduction of apparent activation energy (E_a) to compare the catalytic activity of synthetic materials as catalysts and lower E_a value can make ethane more easily oxidized. According to the

catalyst map of Arrhenius for ethane oxidation (Figure 7D), the E_a values for ethane oxidation increase in the order Fe₂O₃-S (39.7 kJ mol⁻¹) < Fe₂O₃-C (50.9 kJ mol⁻¹) < Fe₂O₃-R (55.3 kJ mol⁻¹) (Table 4), suggesting that ethane is more easily oxidized over Fe₂O₃-S. Table S4 documented some typical catalysts reported in the literature for ethane oxidation. It is shown that 0.98% Co/1.27% Cu-ZSM-5 had a T₅₀ value of 420 °C for ethane combustion,⁵⁰ and TiO₂ had a T₅₀ value greater °C for ethane combustion.⁵¹ Catalysts of than480 La_{0.7}Sr_{0.3}Mn_{0.75}Co_{0.25}O (T₅₀ of 476 °C and T₉₀ of 485 °C)⁵² and La_{0.7}Bi_{0.3}Mn_{0.75}Co_{0.25}O₃ (T₅₀ of 427 °C and T₉₀ of 542 °C)⁵³ were also less active than the Fe₂O₃-S catalyst. Ethane conversion over the Fe₂O₃-S catalyst was even higher than some noble metal loaded catalysts (e.g., T₅₀ and T₉₀ of 425 and 475 °C, respectively, over a reported Pt/Al₂O₃ material).⁵⁵

3.5. Catalytic Stability. Reaction stability is a key criterion for industrial applications. Figure 8A shows that Fe₂O₃-S has excellent ethane combustion stability, and only a slight decrease in ethane conversion from 91 to 88% can be observed in the first 30 h. In addition, the stability of Fe₂O₃-S for ethane destruction at a lower temperature of 360 °C was also studied, as displayed in Figure 8B. We found that Fe₂O₃-S possesses satisfied reaction stability at different temperatures,

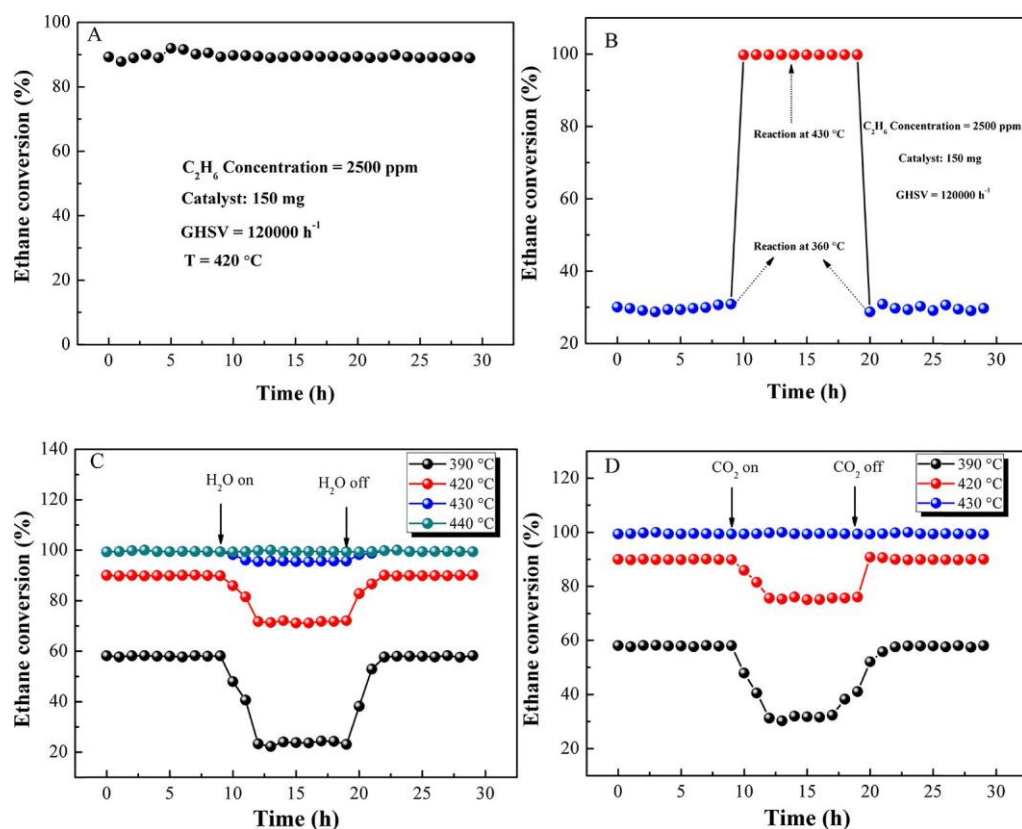


Figure 8. (A, B) Catalytic stability and effect of (C) H₂O and (D) CO₂ on the conversion of ethane over the Fe₂O₃-S catalyst.

and the heating and cooling processes have an insignificant effect on the activity of Fe₂O₃-S. The good stability provides the possibility for the practical elimination of ethane. As shown in Figure S5, the Fe₂O₃-S sample has almost no weight loss in a temperature range of 20–700 °C. The desorption of oxygen and water leading to the weight losses of Fe₂O₃-C (0.2 wt %) and Fe₂O₃-R (0.5 wt %) in a temperature range of 20–100 °C can be attributed to the desorption of H₂O and oxygen,⁵⁴ and no weight loss can be found when the temperature is further increased. Above results indicate the good thermal stability of prepared catalysts. Coke deposition on Fe₂O₃-S after the stability test was further analyzed, as shown in Figure S6. The used sample displays two stages of small weight losses in a temperature range of 20–700 °C. The first one at 20–200 °C (0.3 wt %) can be attributed to the combustion/desorption of adsorbed C₂H₆ and the desorption of O₂ and H₂O, and the second one at 200–700 °C (0.9 wt %) corresponds to the combustion of coke deposited on the catalyst,⁵⁴ which demonstrates that Fe₂O₃-S is an effective catalyst for catalytic oxidation of C₂H₆. The crystal structure of the Fe₂O₃-S catalyst after reaction was determined by XRD, as shown in Figure S7. The diffraction peaks of the used Fe₂O₃-S sample are almost unchanged compared with the fresh sample, indicating that Fe₂O₃-S has a good chemical stability in catalytic reaction.

The influences of H₂O and CO₂ on catalytic activity of prepared materials for ethane destruction were further investigated. Results show that the addition of H₂O (10 vol %) has negative effects on the conversion of ethane (especially at low temperatures (<420 °C)) due to the competition between water and oxygen adsorption on the catalyst surface; however, this negative effect becomes smaller when the reaction temperature is increased, and the influence of H₂O

can be ignored at 440 °C. It is indicated that the deactivation of the catalyst was reversible, and a complete conversion of ethane can be restored when H₂O was no longer added, although recovery took longer at low temperatures.⁵⁶ Similarly, the introduction of CO₂ (10 vol %) also has obvious inhibition effects on ethane conversion, and increase in the reaction temperature can obviously reduce this effect (can be ignored at 430 °C). Moreover, when the addition of CO₂ was stopped, the catalytic activity recovered immediately, whereas a longer time was taken to recover the activity of the catalyst after stopping the addition of water vapor, suggesting that H₂O was adsorbed more strongly than CO₂ to active sites.

4. DISCUSSION

4.1. Adsorption of Ethane. Figure S8 shows the in situ DRIFTS spectra of O₂ and C₂H₆ adsorption on prepared samples at room temperature. The IR bands in the region of 3100–2800 cm⁻¹ can be assigned to the C–H stretching (ν_{CH}) of alkanes or adsorbed C–H bond containing species, and the peaks at 3000–2850 cm⁻¹ can be attributed to the ν_{CH} of C₂H₆.⁵⁷ A broad band with a maximum at 3700–3100 cm⁻¹ belongs to the sorbed water or acidic OH groups that are hydrogen-bonded to the basic oxygen atoms of the catalysts.⁵⁸ It is well known that stretching bands for gaseous ethane were at 2954 and 2994 cm⁻¹.⁵⁹ Table S3 reveals that the position of C–H stretching bands for adsorbed ethane over Fe₂O₃-S, Fe₂O₃-C, and Fe₂O₃-R samples is similar, while all the bands are red-shifted to some extent in comparison with those of gaseous ethane due to a combination of ligand-to-metal electron donation from the C–H σ-bond to vacant Fe³⁺ s-orbit combined with the metal-to-ligand back donation from the iron dπ-orbital to C–H σ*-orbital because these interactions lead

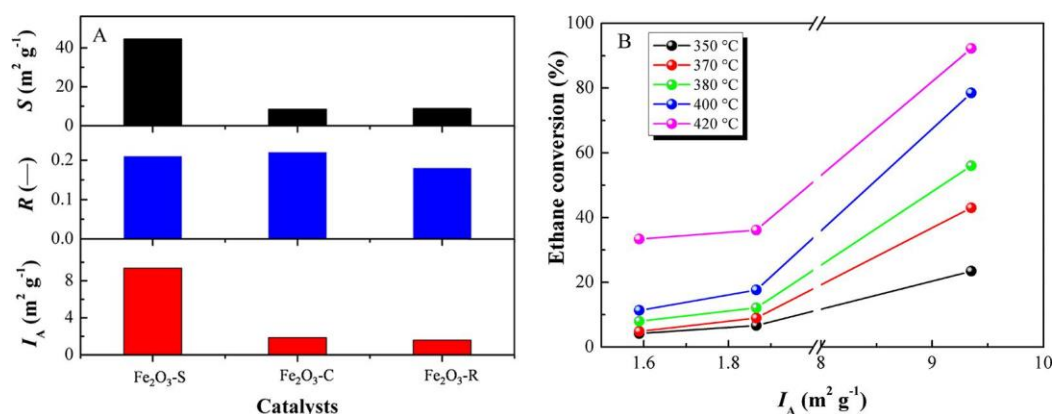


Figure 9. (A) Correlation between S, R, and I_A. (B) Relation between the conversion of ethane and index I_A for all catalysts.

to a very marked weakening of the C–H bond.^{59,60} It has been proved that the adsorption of light alkanes by metal oxides in the form of cations results in the change of relative intensity distribution of absorption bands, which largely depends on the properties of cations and metallic oxides.⁶⁰ According to the adsorption strength of ethane on all samples, it is found that Fe₂O₃-C is easier to adsorb water than ethane. However, compared with water, it has stronger adsorption for ethane on Fe₂O₃-S and Fe₂O₃-R. It is also shown that the strongest perturbation and polarization oscillations are initially fully symmetrical C–H stretching oscillations, which are directly related to the chemical activation of adsorbed molecules.⁶¹ The greatest red shift of the C–H band was observed for C₂H₆ adsorption on Fe₂O₃-S. This means that Fe₂O₃-S has stronger chemical activation for ethane molecules.⁶¹

Figure S9 shows the in situ DRIFT spectra of ethane and air adsorption over synthesized catalysts at different temperatures. The intensity of bands at 3700–3100 cm⁻¹ shows a continuous reduction (disappeared at 150 °C) when increasing the temperature, indicating the removal of sorbed water from materials.⁶² It should be noted that the intensity variation of bands at 3100–2800 cm⁻¹ assigned to the C–H stretching (ν_{CH}) of alkanes or adsorbed C–H bond containing species over Fe₂O₃-S (even visible at 200 °C) is much smaller than those over Fe₂O₃-C and Fe₂O₃-R materials, suggesting the strongest ethane adsorption (dissociative adsorption) over the Fe₂O₃-S sample. As shown in Figure S9, for Fe₂O₃-S, the intensity of the bands in the region of 2800–3100 cm⁻¹ is the strongest among all samples, indicating that ethane adsorbed on Fe₂O₃-S has a lower activation barrier.⁶³

4.2. Correlation of Physicochemical Property and Activity. Specific surface area, concentration and distribution of reactive oxygen species, surface defects and oxygen vacancies, and catalyst reducibility can affect its catalytic performance in oxidation reaction. Zheng et al.⁸ proved that the high density of Fe atoms on the exposure {110} planes of α-Fe₂O₃ leads to high activity for catalytic combustion of CO. Kameoka et al.⁵⁶ stated that surface Fe sites on La_{1-x}Sr_xFeO₃ (x = 0.0–1.0) perovskites are an active species for methane combustion.

Kouotou et al.¹ proved that the more iron content in α-Fe₂O₃ exposed planes, the more active sites for catalytic for catalytic combustion of propene. As it is known, the density of active sites such as the iron atoms is different over various exposed planes in a hematite crystal structure. Table 1 shows that the specific surface area of prepared catalysts and the

surface metal compositions obtained from XPS analysis are included in Figure 9. Fe/(Fe + O), defined as the R ratio, is an important factor representing α-Fe₂O₃ catalyst activity. Surface area plays a role in catalyst activity, the product of the BET surface area (S) and R, defined as the index I_A.⁵⁶ It is worth noting that the content of iron atoms over all catalysts is smaller than two-thirds because all catalysts adsorbed a large amount of oxygen on their surface. Figure 9 shows the relationships of different parameters (S, R, and I_A; I_A and ethane conversion) of different catalysts, and results indicate that the surface Fe content over catalysts is directly proportional to the conversion of ethane. Fe₂O₃-S has a maximum I_A value (9.35 m² g⁻¹) and has the highest catalytic activity for catalytic oxidation of ethane.

The Mars van Krevelen (MVK) mechanism has been widely used in interpreting the catalytic oxidation process of hydrocarbons, especially for hydrocarbon oxidation over transition metal oxides, which involves a redox cycle (migration of bulk oxygen to the catalyst surface to oxidize hydrocarbon molecules and replace the bulk oxygen by oxygen from the gas phase) and is closely related to the mobility of the lattice oxygen.¹ As such, the oxygen mobility associated with catalyst reducibility is an important factor for the MVK mechanism.⁶⁴ Taking into account the TPR results, it can be concluded that the lattice oxygen mobility in the prepared samples is in the order of Fe₂O₃-S > Fe₂O₃-C > Fe₂O₃-R. High lattice oxygen mobility can accelerate the redox cycle in ethane oxidation and guarantee the superior activity of Fe₂O₃-S. On the basis of the MVK mechanism and in situ DRIFTS results displayed in Figure S8, a reaction scheme for ethane oxidation was proposed: First, ethane is considered to be adsorbed dissociatively on the surface of the catalyst with extraction of a hydrogen atom and then the release of oxygen atom along with the reduction of the catalyst. Finally, oxygen from the gas phase will reoxidize the reduced iron cations to Fe₂O₃.⁶⁵

XPS results reveal that the percentage of O_β on the Fe₂O₃-S catalyst (0.72) is higher than those of Fe₂O₃-C (0.59) and Fe₂O₃-R (0.55), indicating that Fe₂O₃-S possesses higher concentration of chemisorbed oxygen species, which leads to higher proportion of Fe³⁺ in Fe₂O₃-S and has generated more oxygen vacancies (Figure 9).⁶⁶ Results of EELS (Figure 6) and Raman (Figure 4) also suggest that the concentration of oxygen vacancies on Fe₂O₃-S is higher than those of Fe₂O₃-C and Fe₂O₃-R. Above results indicate that the Fe₂O₃-S sample can produce more reactive oxygen species participating in the oxidation of ethane. Additionally, Mössbauer spectroscopy and Raman

results reveal that there are more defect sites over F2O3-S than F2O3-C and F2O3-R samples, which enhance the oxygen transfer and reduction efficiency, promoting the ethane oxidation rate.⁶⁶

4.3. Formation Energy of Oxygen Vacancy. Oxygen vacancies are suggested to play an important role in the decomposition of ethane, and its activity much rests with the nature of oxygen vacancy.⁶⁷ In the present work, the formation energy of a single O defect at α -Fe2O3 exposed facets is studied by DFT calculations, as shown in Figure 10. Results

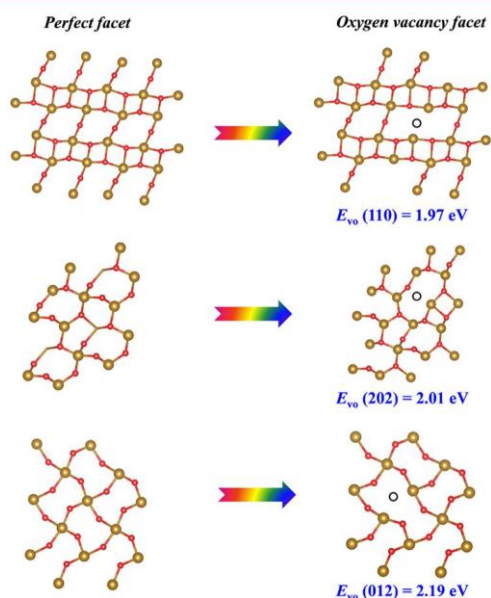


Figure 10. Formation energy of oxygen vacancy over α -Fe2O3 with different exposed facets.

demonstrate that the formation energy of oxygen vacancy on the (110) facet ($E_{VO}(110) = 1.97$ eV) is lower than those of (202) facet ($E_{VO}(202) = 2.01$ eV) and (012) facet ($E_{VO}(012) = 2.19$ eV), indicating that the oxygen vacancies are more

easier to form on (110) facets of F2O3-S (consistent with the in situ Raman results (Figure S2)), endowing the superior ethane destruction activity of the F2O3-S catalyst.

4.4. Adsorption of O2, C2H6, and H2O on Exposed Facets. The O2 adsorption capability is a very important parameter for VOC oxidation reactions according to the MVK mechanism. As such, the adsorption energy of O2 on different perfect facets and facets with oxygen vacancies was obtained by DFT (Figure 11). The perfect facets of (110), (202), and (12) have an analogous adsorption capacity for oxygen, and the adsorption energy is very small (0.2 eV); it shows that the adsorption of O2 on all perfect facets showed very weak physical adsorption. However, when the oxygen vacancy is introduced to the crystal surface, the adsorption energy of molecular O2 on all facets becomes higher, which indicates that oxygen vacancy is more conducive to catalytic oxidation of ethane. The adsorption energies of O2 on facets with oxygen vacancies of (110), (202), and (012) are 1.58, 1.55 and 1.22 eV, respectively (Figure 11), indicating that O2 is easily adsorbed on the face of (110). In addition, the (110) surface is strongly bonded with O2 with the O-O bond distance, which is 1.405 Å. The longer bond length than this on the (202) (1.394 Å) and (012) (1.371 Å) facets indicates that O2 can be destroyed more and activated easily. The strong adsorption of O2 on the (110) surface facilitates the quick addition of oxygen consumed by the oxidation reaction and is beneficial to the catalytic oxidation of ethane. The corresponding adsorption energies of ethane on (110), (202), and (012) surfaces were calculated to be -0.26, -0.23, and -0.21 eV, respectively (Figure S10), in good accordance to the order of catalytic performance of prepared materials. In addition, the adsorption energy of water on the (110) surface is calculated. As shown in Figure S11, we found that the adsorption energy of H2O (-1.54 eV) is close to that of O2 (-1.58 eV), suggesting the reason for the competition between water and oxygen adsorption on the surface of the catalyst.

Figure 12 shows the total electronic density of states (DOS) and its projections over the 3d orbitals of iron cations and the 2p orbitals of the O anions for (110), (202), and (012)

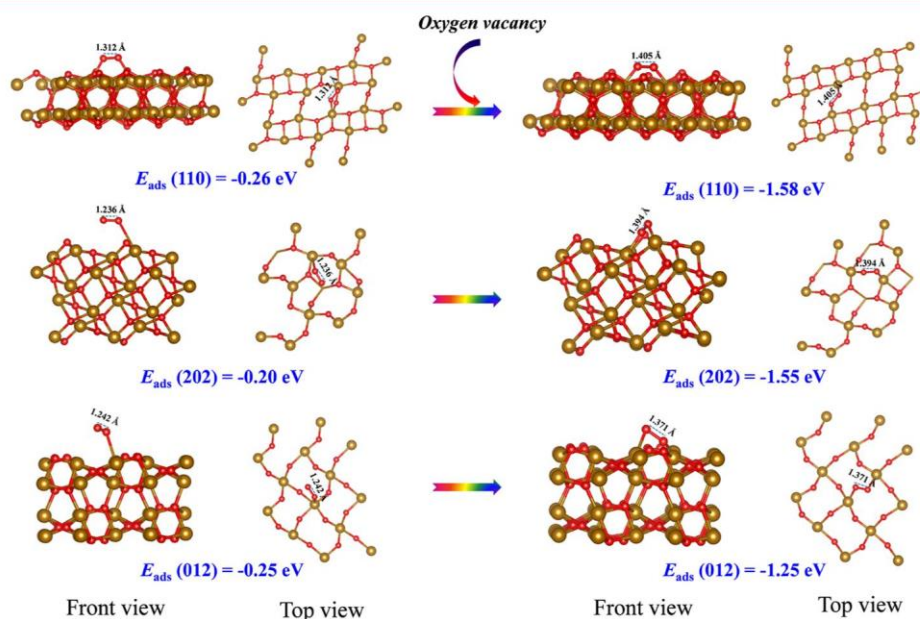


Figure 11. Adsorption energy of O2 over α -Fe2O3 with different exposed perfect crystal surfaces and crystal surfaces with oxygen vacancies.

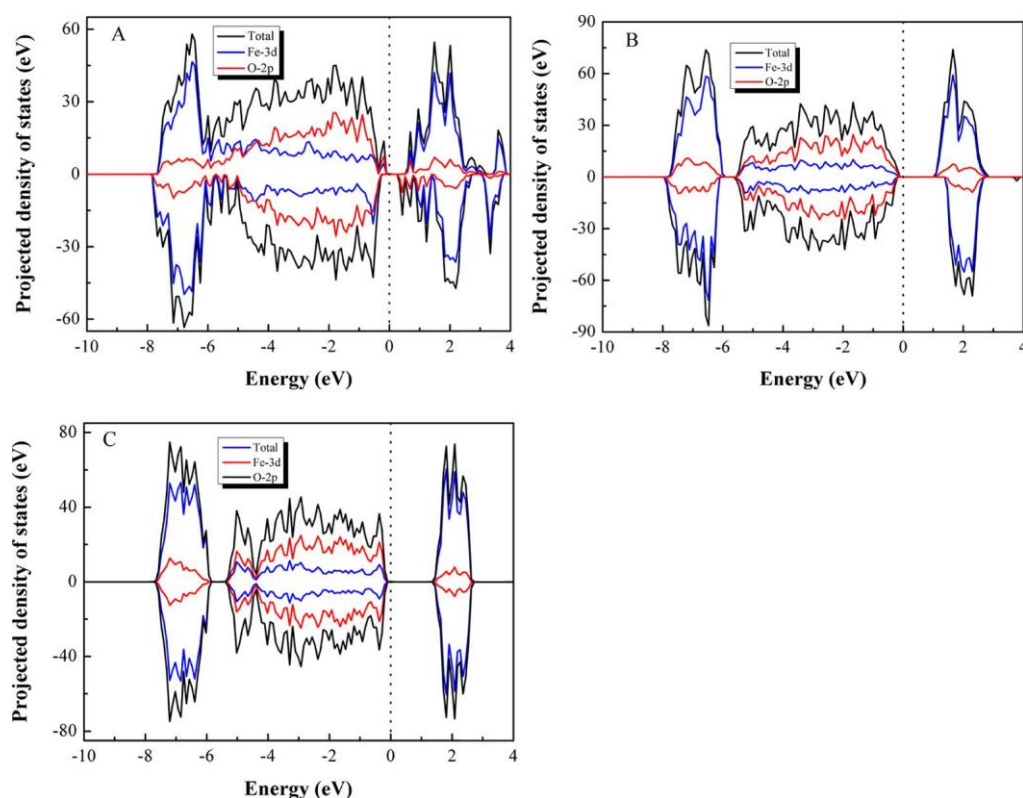


Figure 12. Projected density of states (PDOS) of different catalysts: (A) Fe₂O₃-S, (B) Fe₂O₃-C, and (C) Fe₂O₃-R (Fe 3d and O 2p states are plotted as solid and dotted lines, respectively). The Fermi energy is set to be 0, highlighted by a black vertical dashed line.

surfaces of α -Fe₂O₃.⁶⁸ For all samples, the top of the valence band is mainly of O 2p character, while the occupied 3d levels of Fe lie around 6–8 eV below the Fermi level. The unoccupied 3d levels of Fe, which have an octahedral coordination, mainly populate the bottom of the conduction band.⁶⁸ As such, maghemite is a charge transfer-type insulator, and the first excitation term should correspond to the transfer of electrons from O²⁻ anions to octahedral Fe³⁺ cations.⁶⁸ Furthermore, the existence of some of these surface states in the bulk band gap indicates the variation of metal characteristics in all of these models.⁶⁸ By gathering the DOSs of surface ions, the (110) surface shows the highest metallic behavior with a narrow band gap of 0.26 eV compared to the (202) and

(12) surfaces with band gaps of about 1.11 and 1.46 eV, respectively. These results highlight the promising role of the (110) surface of α -Fe₂O₃ in surface redox reactions.

For the (110) surface, the electronic state covers most of the bulk band gap regions and shows higher polarity on the surface than other regions because the stabilization of the polarized surface can be achieved by the depolarization field, which causes some changes in the electronic surface state so that some states appear in the bulk band gap region.⁶⁸ Subsequently, neutralization of the polarized surfaces can be obtained by the flow of free charge within the surface layer.⁶⁸ The (110) surface shows the highest metal features with a very narrow band gap. Furthermore, these states can provide a depolarizing field, which has a vital role in the stabilization of the polar termination.⁶⁸

Finally, the (100) surfaces are more polar than stoichiometry, which cause a relatively low stability of these models. It is indicated that the (110) surface is more likely to lose electrons, which makes it easier for oxidation–reduction reactions.

5. CONCLUSIONS

In summary, α -Fe₂O₃ samples with different morphologies were successfully synthesized by the simple solvothermal method. Fe₂O₃-S exhibits superior catalytic activity in the oxidation of ethane due to its highest low-temperature reducibility and largest number of active surface lattice defects and oxygen vacancies. Theoretical calculations confirm that the exposed (110) facet has the lowest oxygen vacancy formation energy (1.97 eV), which is favorable for the formation of surface active oxygen species. In addition, the exposed (110) facets facilitate the adsorption and activation of O₂ ($E_{\text{ads}} = -1.58$ eV; bond length of adsorbed O₂ is 1.405 Å, which is far greater than the distances of 1.394 and 1.371 Å for (202) and (12) facets) and an easier redox process, which promotes the ethane oxidation activity. These results can provide a simple and effective strategy for the engineering design of reaction exposed surfaces and deepen the understanding of the small side-related catalytic activity of α -Fe₂O₃ in hydrocarbon destruction.

ASSOCIATED CONTENT

N₂ adsorption–desorption isotherms and pore size distribution, intensity of the fitted E_g , LO, and T bands present in the Raman spectra, in situ Raman spectra, TPR profiles, in situ DRIFTS spectra of ethane adsorption, summary of some active catalysts for ethane oxidation, and adsorption energy of ethane and H₂O on catalysts (PDF)

AUTHOR INFORMATION

Corresponding Author

*E-mail: chi_he@xjtu.edu.cn. Tel.: +86 29 82663857. Fax: +86 29 82663857.

ORCID

Yanke Yu: 0000-0003-4214-8284

Chi He: 0000-0001-6403-1277

Author Contributions

[○]Y.J. and T.Y. contributed equally to this work.

Notes

The authors declare no competing financial interest.

ACKNOWLEDGMENTS

This work was financially supported by the National Natural Science Foundation of China (21677114, 21876139, and 21477095), the National Key Research and Development Program (2016YFC0204201), and the Fundamental Research Funds for the Central Universities (xjj2017170). The valuable comments from the editor and anonymous reviewers are much appreciated.

REFERENCES

- (1) Kouotou, P. M.; Tian, Z.-Y.; Vieker, H.; Beyer, A.; Gölzhauser, A.; Kohse-Höinghaus, K. Selective Synthesis of α -Fe₂O₃ thin Films and Effect of the Deposition Temperature and Lattice Oxygen on the Catalytic Combustion of Propene. *J. Mater. Chem. A* 2013, 1, 10495–10504.
- (2) Alifantii, M.; Bueno, G.; Parvulescu, V.; Parvulescu, V. I.; Cortes Corberan, V. Oxidation of Ethane on High Specific Surface SmCoO₃ and PrCoO₃ Perovskites. *Catal. Today* 2009, 143, 309–314.
- (3) Suarez-Vazquez, S. I.; Gil, S.; García-Vargas, J. M.; Cruz-Lopez, A.; Giroir-Fendler, A. Catalytic Oxidation of Toluene by SrTi_{1-x}BxO₃ (B = Cu and Mn) With Dendritic Morphology Synthesized by One Pot hydrothermal Route. *Appl. Catal., B* 2018, 223, 201–208.
- (4) He, C.; Jiang, Z.; Ma, M.; Zhang, X.; Douthwaite, M.; Shi, J.-W.; Hao, Z. Understanding the Promotional Effect of Mn₂O₃ on Micro-/ Mesoporous Hybrid Silica Nanocubic-Supported Pt Catalysts for the Low-Temperature Destruction of Methyl Ethyl Ketone: An Experimental and Theoretical Study. *ACS Catal.* 2018, 8, 4213–4229.
- (5) Liu, J.; Meeprasert, J.; Namuangruk, S.; Zha, K.; Li, H.; Huang, L.; Maitarad, P.; Shi, L.; Zhang, D. Facet-Activity Relationship of TiO₂ in Fe₂O₃/TiO₂ Nanocatalysts for Selective Catalytic Reduction of NO with NH₃: In Situ DRIFTS and DFT Studies. *J. Phys. Chem. C* 2017, 121, 4970–4979.
- (6) He, C.; Cheng, J.; Zhang, X.; Douthwaite, M.; Pattison, S.; Hao, Z. Recent Advances in the Catalytic Oxidation of Volatile Organic Compounds: A Review Based on Pollutant Sorts and Sources. *Chem. Rev.* 2019, DOI: 10.1021/acs.chemrev.8b00408.
- (7) Hu, X.; Huang, L.; Zhang, J.; Li, H.; Zha, K.; Shi, L.; Zhang, D. Facile and Template-free Fabrication of Mesoporous 3D Nanosphere-like Mn_xCo_{3-x}O₄ as Highly Effective Catalysts for Low Temperature SCR of NO_x with NH₃. *J. Mater. Chem. A* 2018, 6, 2952–2963.
- (8) Zheng, Y. H.; Cheng, Y.; Wang, Y. S.; Bao, F.; Zhou, L. H.; Wei, X. F.; Zhang, Y. Y.; Zheng, Q. Quasicubic α -Fe₂O₃ Nanoparticles with Excellent Catalytic Performance. *J. Phys. Chem. B* 2006, 110, 3093–3097.
- (9) Jian, Y.; Ma, M.; Chen, C.; Liu, C.; Yu, Y.; Hao, Z.; He, C. Tuning the Micromorphology and Exposed Facets of MnO_x Promotes Methyl Ethyl Ketone Low-temperature Abatement: Boosting Oxygen Activation and Electron Transmission. *Catal. Sci. Technol.* 2018, 8, 3863–3875.
- (10) Rong, S.; Zhang, P.; Liu, F.; Yang, Y. Engineering Crystal Facet of α -MnO₂ Nanowire for Highly Efficient Catalytic Oxidation of Carcinogenic Airborne Formaldehyde. *ACS Catal.* 2018, 8, 3435–3446.
- (11) Yao, W.-T.; Yu, S.-H.; Wu, Q.-S. From Mesostructured Wurtzite ZnS-nanowire/amine Nanocomposites to ZnS Nanowires Exhibiting Quantum Size Effects: A Mild-solution Chemistry Approach. *Adv. Funct. Mater.* 2007, 17, 623–631.
- (12) Wang, C.; Hou, Y.; Kim, J.; Sun, S. A General Strategy for Synthesizing FePt Nanowires and Nanorods. *Angew. Chem., Int. Ed.* 2007, 46, 6333–6335.
- (13) Bachmann, J.; Jing, J.; Knez, M.; Barth, S.; Shen, H.; Mathur, S.; Gosele, U.; Nielsch, K. Ordered Iron Oxide Nanotube Arrays of Controlled Geometry and Tunable Magnetism by Atomic Layer Deposition. *J. Am. Chem. Soc.* 2007, 129, 9554–9555.
- (14) Zhang, L.; Ruh, E.; Grützmaier, D.; Dong, L.; Bell, D. J.; Nelson, B. J.; Schonenberger, C. Anomalous Coiling of SiGe/Si and SiGe/Si/Cr Helical Nanobelts. *Nano Lett.* 2006, 6, 1311–1317.
- (15) Xu, L. Q.; Zhan, J. H.; Hu, J. Q.; Bando, Y.; Yuan, X. L.; Sekiguchi, T.; Mitome, M.; Golberg, D. High-yield Synthesis of Rhombohedral Boron Nitride Triangular Nanoplates. *Adv. Mater.* 2007, 19, 2141–2144.
- (16) Paek, J.; Lee, C. H.; Choi, J.; Choi, S.-Y.; Kim, A.; Lee, J. W.; Lee, K. Gadolinium Oxide Nanoring and Nanoplate: Anisotropic Shape Control. *Cryst. Growth Des.* 2007, 7, 1378–1380.
- (17) Zhou, K.; Wang, X.; Sun, X.; Peng, Q.; Li, Y. Enhanced Catalytic Activity of Ceria Nanorods from Well-defined Reactive Crystal Planes. *J. Catal.* 2005, 229, 206–212.
- (18) Chen, A.; Zhou, Y.; Ta, N.; Li, Y.; Shen, W. Redox Properties and Catalytic Performance of Ceria-zirconia Nanorods. *Catal. Sci. Technol.* 2015, 5, 4184–4192.
- (19) Xie, Y.; Yu, Y.; Gong, X.; Guo, Y.; Guo, Y.; Wang, Y.; Lu, G. Effect of the Crystal Plane Figure on the Catalytic Performance of MnO₂ for the Total Oxidation of Propane. *CrystEngComm* 2015, 17, 3005–3014.
- (20) Qiu, G.; Huang, H.; Genuino, H.; Opembe, N.; Stafford, L.; Dharmarathna, S.; Suib, S. L. Microwave-Assisted Hydrothermal Synthesis of Nanosized α -Fe₂O₃ for Catalysts and Adsorbents. *J. Phys. Chem. C* 2011, 115, 19626–19631.
- (21) Yoo, S.-G.; Kim, J.-H.; Kim, U.-H.; Jung, J.-S.; Lee, S.-H. Comparison of the Kinetic Behaviors of Fe₂O₃ Spherical Submicron Clusters and Fe₂O₃ Fine Powder Catalysts for CO Oxidation. *Bull. Korean Chem. Soc.* 2014, 35, 1379–1384.
- (22) Wu, J.; Su, T.; Jiang, Y.; Xie, X.; Qin, Z.; Ji, H. In situ DRIFTS Study of O₃ Adsorption on CaO, γ -Al₂O₃, CuO, α -Fe₂O₃ and ZnO at Room Temperature for the Catalytic Ozonation of Cinnamaldehyde. *Appl. Surf. Sci.* 2017, 412, 290–305.
- (23) Ramezani, Z.; Shekarriz, M.; Behfar, A. A.; Kiamarzi, S. Pre-Concentration and Separation of Perphenazine Using Picric Acid Loaded α -Fe₂O₃ Nanoparticles: HPLC Syringe Filter as the Particles Support. *J. Braz. Chem. Soc.* 2017, 28, 2172–2179.
- (24) Larcher, D.; Sudant, G.; Patrice, R.; Tarascon, J. M. Some Insights on the Use of Polyols-based Metal Alkoxides Powders as Precursors for Tailored Metal-oxides Particles. *Chem. Mater.* 2003, 15, 3543–3551.
- (25) Fang, J.; Xu, J.; Chen, J.; Huang, X.; Wang, X. Enhanced Photocatalytic Activity of Molecular Imprinted Nano α -Fe₂O₃ by Hydrothermal Synthesis Using Methylene Blue as Structure-directing Agent. *Colloids Surf., A* 2016, 508, 124–134.
- (26) Liu, A.; Xia, Z.; Zhou, W.; Huang, S. Well-dispersed Hematite Nanoparticles Decorating Graphene Nanosheets: Characterization and Performance for Methyl Orange Removal. *J. Environ. Chem. Eng.* 2017, 5, 6039–6044.
- (27) Wang, J.; Wang, C.; Tong, S. A novel composite Fe-N/O Catalyst for the Effective Enhancement of Oxidative Capacity of Persulfate at Ambient Temperature. *Catal. Commun.* 2018, 103, 105–109.
- (28) Xie, P.; Ma, Z.; Meng, T.; Huang, C.; Miao, C.; Yue, Y.; Hua, W.; Gao, Z. Active Fe Species of Fe₂O₃/Fe-Silicalite-1 Nanowires in N₂O Decomposition. *J. Mol. Catal. A: Chem.* 2015, 409, 50–58.
- (29) Tirupanyam, B. V.; Srinivas, C.; Meena, S. S.; Yusuf, S. M.; Satish Kumar, A.; Sastry, D. L.; Seshubai, V. Investigation of Structural and Magnetic Properties of Co-precipitated Mn-Ni Ferrite

- Nanoparticles in the Presence of α -Fe₂O₃ Phase. *J. Magn. Magn. Mater.* 2015, 392, 101–106.
- (30) Nag, S.; Roychowdhury, A.; Ds, D.; Mukherjee, S. Synthesis of α -Fe₂O₃-functionalised Graphene Oxide Nanocomposite by a Facile Low Temperature Method and Study of its Magnetic and Hyperfine Properties. *Mater. Res. Bull.* 2016, 74, 109–116.
- (31) Idczak, R.; Konieczny, R.; Chojcan, J. Study of defects in Fe–Re and Fe–Mo Alloys by the Mössbauer and Positron Annihilation Spectroscopies. *Solid State Commun.* 2012, 152, 1924–1928.
- (32) Cheng, X.; Li, K.; Wei, Y.; Zhu, X.; Tian, D. Modification of KNO₃ on the reducibility and reactivity of Fe₂O₃-based oxygen carriers for chemical-looping combustion of methane. *Can. J. Chem. Eng.* 2017, 95, 1569–1578.
- (33) Almeida, T. P.; Fay, M. W.; Zhu, Y.; Brown, P. D. Hydrothermal Growth Mechanism of α -Fe₂O₃ Nanorods Derived by Near in Situ Analysis. *Nanoscale* 2010, 2, 2390–2399.
- (34) Guo, Y.; Zhang, S.; Zhu, J.; Su, L.; Xie, X.; Li, Z. Effects of Pt on Physicochemical Properties over Pd Based Catalysts for Methanol Total Oxidation. *Appl. Surf. Sci.* 2017, 416, 358–364.
- (35) Zhou, H.; Li, K.; Zhao, B.; Deng, W.; Su, Y.; Zhong, F. Surface Properties and Reactivity of Fe/Al₂O₃/cordierite Catalysts for NO Reduction by C₂H₆: Effects of calcination temperature. *Chem. Eng. J.* 2017, 326, 737–744.
- (36) Cardillo, D.; Tehei, M.; Hossain, S.; Islam, M.; Bogusz, K.; Shi, D.; Mitchell, D.; Lerch, M.; Rosenfeld, A.; Corde, S.; Konstantinov, K. Synthesis-Dependent Surface Defects and Morphology of Hematite Nanoparticles and Their Effect on Cytotoxicity in Vitro. *ACS Appl. Mater. Interfaces* 2016, 8, 5867–5876.
- (37) Grosvenor, A. P.; Kobe, B. A.; Biesinger, M. C.; McIntyre, N. S. Investigation of Multiplet Splitting of Fe 2p XPS Spectra and Bonding in Iron Compounds. *Surf. Interface Anal.* 2004, 36, 1564–1574.
- (38) Chernyshova, I. V.; Hochella, M. F., Jr.; Madden, A. S. Size-Dependent Structural Transformations of Hematite Nanoparticles. I. Phase Transition. *Phys. Chem. Chem. Phys.* 2007, 9, 1736–1750.
- (39) Łojewska, J.; Knapik, A.; Kołodziej, A.; Jodłowski, P. Far Field Combined AFM and Micro-Raman Imaging for Characterisation of Surface of Structured Catalysts: Example of Pd Doped CoO_x Catalysts on Pre-calcined Kanthal Steel. *Top. Catal.* 2013, 56, 1088–1095.
- (40) Chen, J.; Chen, X.; Xu, W.; Xu, Z.; Chen, J.; Jia, H.; Chen, J. Hydrolysis Driving Redox Reaction to Synthesize Mn-Fe Binary Oxides as Highly Active Catalysts for the Removal of Toluene. *Chem. Eng. J.* 2017, 330, 281–293.
- (41) Lin, X.; Li, S.; He, H.; Wu, Z.; Wu, J.; Chen, L.; Ye, D.; Fu, M. Evolution of Oxygen Vacancies in MnO_x-CeO₂ Mixed Oxides for Soot Oxidation. *Appl. Catal., B* 2018, 223, 91–102.
- (42) Tsoncheva, T.; Ivanova, R.; Dimitrov, M.; Paneva, D.; Kovacheva, D.; Hnych, J.; Vomacka, P.; Kormunda, M.; Velinov, N.; Mitov, I.; Stengl, V. Template-assisted Hydrothermally Synthesized Iron-titanium Binary Oxides and their Application as Catalysts for Ethyl Acetate Oxidation. *Appl. Catal., A* 2016, 528, 24–35.
- (43) Chueh, Y.-L.; Lai, M.-W.; Liang, J.-Q.; Chou, L.-J.; Wang, Z.-L. Systematic Study of the Growth of Aligned Arrays of α -Fe₂O₃ and Fe₃O₄ Nanowires by a Vapor–Solid Process. *Adv. Funct. Mater.* 2006, 16, 2243–2251.
- (44) Colliex, C.; Manoubi, T.; Ortiz, C. Electron-energy-loss-spectroscopy Near-edge Fine structures in the Iron-oxygen System. *Phys. Rev. B* 1991, 44, 11402–11411.
- (45) Alshehri, A. A.; Narasimharao, K. Low Temperature Oxidation of Carbon Monoxide over Mesoporous Au-Fe₂O₃ Catalysts. *J. Nanomater.* 2017, 2017, 1–14.
- (46) Wang, F.; Dai, H.; Deng, J.; Bai, G.; Ji, K.; Liu, Y. Manganese Oxides With Rod-, Wire-, Tube-, and Flower-like Morphologies: Highly Effective Catalysts for the Removal of Toluene. *Environ. Sci. Technol.* 2012, 46, 4034–4041.
- (47) Wang, Z.; Wang, W.; Zhang, L.; Jiang, D. Surface Oxygen Vacancies on Co₃O₄ Mediated Catalytic Formaldehyde Oxidation at Room Temperature. *Catal. Sci. Technol.* 2016, 6, 3845–3853.
- (48) Liu, Q.; Wang, L.-C.; Chen, M.; Cao, Y.; He, H.-Y.; Fan, K.-N. Dry Citrate-precursor Synthesized Nanocrystalline Cobalt Oxide as Highly Active Catalyst for Total Oxidation of Propane. *J. Catal.* 2009, 263, 104–113.
- (49) Kucherov, A. V.; Hubbard, C. P.; Kucherova, T. N.; Shelef, M. Stabilization of the Ethane Oxidation Catalytic Activity of Cu-ZSM-5. *Appl. Catal., B* 1996, 7, 285–298.
- (50) Tahir, S. F.; Koh, C. A. Catalytic Oxidation for Air Pollution Control. *Environ. Sci. Pollut. Res.* 1996, 3, 20–23.
- (51) Gholizadeh, A.; Malekzadeh, A.; Ghiasi, M. Structural and Magnetic Features of La_{0.7}Sr_{0.3}Mn_{1-x}Co_xO₃ Nano-catalysts for Ethane Combustion and CO Oxidation. *Ceram. Int.* 2016, 42, 5707–5717.
- (52) Gholizadeh, A.; Malekzadeh, A. Structural and Redox Features of La_{0.7}Bi_{0.3}Mn_{1-x}Co_xO₃ Nanoperovskites for Ethane Combustion and CO Oxidation. *Int. J. Appl. Ceram. Technol.* 2017, 14, 404–412.
- (53) Dadi, R. K.; Luss, D.; Balakotaiah, V. Dynamic Hysteresis in Monolith Reactors and Hysteresis Effects During Co-oxidation of CO and C₂H₆. *Chem. Eng. J.* 2016, 297, 325–340.
- (54) Fareghi-Alamdari, R.; Niri, M. N.; Hazarkhani, H.; Zekri, N. Diacidic ionic Liquid Supported on Magnetic-silica Nanocomposite: a Novel, Stable, and Reusable Catalyst for Selective Diester Production. *J. Iran. Chem. Soc.* 2018, 15, 2615–2629.
- (55) Wang, C.-H.; Chen, C.-L.; Weng, H.-S. Surface Properties and Catalytic Performance of La_{1-x}Sr_xFeO₃ Perovskite-type Oxides for Methane Combustion. *Chemosphere* 2004, 57, 1131–1138.
- (56) Kameoka, S.; Kita, K.; Tanaka, S.-I.; Nobukawa, T.; Ito, S.-i.; Tomishige, K.; Miyadera, T.; Kunimori, K. Enhancement of C₂H₆ Oxidation by O₂ in the Presence of N₂O Over Fe ion-exchanged BEA Zeolite Catalyst. *Catal. Lett.* 2002, 79, 63–67.
- (57) Kazansky, V. B.; Pidko, E. A. Intensities of IR Stretching Bands as a Criterion of Polarization and Initial Chemical Activation of Adsorbed Molecules in Acid Catalysis. Ethane Adsorption and Dehydrogenation by Zinc ions in ZnZSM-5 Zeolite. *J. Phys. Chem. B* 2005, 109, 2103–2108.
- (58) Kazansky, V. B.; Subbotina, I. R.; Jentoft, F. C.; Schlogl, R. Intensities of C–H IR Stretching Bands of Ethane and Propane Adsorbed by Zeolites as a New Spectral Criterion of their Chemical Activation via Polarization Resulting from Stretching of Chemical Bonds. *J. Phys. Chem. B* 2006, 110, 17468–17477.
- (59) Pidko, E.; Kazansky, V. σ -Type Ethane Adsorption Complexes with Cu⁺ ions in Cu(i)-ZSM-5 Zeolite. Combined DRIFTS and DFT Study. *Phys. Chem. Chem. Phys.* 2005, 7, 1939–1944.
- (60) Shilina, M. I.; Vasilevskii, G. Y.; Rostovshchikova, T. N.; Murzin, V. Y. Unusual Coordination State of Cobalt ions in Zeolites Modified by Aluminum Chloride. *Dalton Trans.* 2015, 44, 13282–13293.
- (61) Pirayavaraporn, C.; Rades, T.; Gordon, K. C.; Tucker, I. G. Quantification of the Types of Water in Eudragit RLPO Polymer and the Kinetics of Water Loss using FTIR. *Int. J. Pharm.* 2013, 458, 90–98.
- (62) Kazansky, V. B.; Subbotina, I. R.; Pronin, A. A.; Schlogl, R.; Jentoft, F. C. Unusual infrared spectrum of ethane adsorbed by gallium oxide. *J. Phys. Chem. B* 2006, 110, 7975–7978.
- (63) Pan, H.; Jian, Y.; Chen, C.; He, C.; Hao, Z.; Shen, Z.; Liu, H. Sphere-Shaped Mn₃O₄ Catalyst with Remarkable Low-Temperature Activity for Methyl-Ethyl-Ketone Combustion. *Environ. Sci. Technol.* 2017, 51, 6288–6297.
- (64) Karamullaoglu, G.; Dogu, T. Oxidative Dehydrogenation of Ethane Over a Monolith Coated by Molybdenum-vanadium-niobium Mixed-oxide Catalyst. *Chem. Eng. Commun.* 2003, 190, 1427–1438.
- (65) Tan, H.; Wang, J.; Yu, S.; Zhou, K. Support Morphology-Dependent Catalytic Activity of Pd/CeO₂ for Formaldehyde Oxidation. *Environ. Sci. Technol.* 2015, 49, 8675–8682.
- (66) Zhu, L.; Wang, J.; Rong, S.; Wang, H.; Zhang, P. Cerium Modified Birnessite-type MnO₂ for Gaseous Formaldehyde Oxidation at Low Temperature. *Appl. Catal., B* 2017, 211, 212–221.
- (67) Grau-Crespo, R.; Al-Baitai, A. Y.; Saadoun, I.; De Leeuw, N. H. Vacancy Ordering and Electronic Structure of gamma-Fe₂O₃ (maghemite): a Theoretical Investigation. *J. Phys.: Condens. Matter* 2010, 22, 255401.

(68) Hashim, A. H.; Zayed, A. O. H.; Zain, S. M.; Lee, V. S.; Said, S. M. Electronic, Magnetic and Structural Properties of Co_3O_4 (100) Surface: a DFT+U Study. *Appl. Surf. Sci.* 2018, 427, 1090–1095.